A Model Predictive Controlled Bidirectional Four Quadrant Flying Capacitor DC/DC Converter Applied in Energy Storage System

Kaitao Bi, Huayang Lv, Liang Chen, Jianfei Li, Yixin Zhu, *Senior Member, IEEE*,
Wentao Huang, and Qigao Fan, *Member, IEEE*

***Abstract*—Energy storage system (ESS) has been widely used in photovoltaic system to ensure stable power generation. This article proposes a flying capacitor bidirectional buck–boost converter (FCBBC), aiming at making the ESS work with bidirectional four quadrant in the wide dc+bus voltage variation condition. With the symmetrical modulation strategy, the proposed FCBBC can achieve seamless switching between buck and boost mode to match the voltage changes at energy storage and dc bus side. Meanwhile, considering the ESS application requirements, a fixed frequency model predictive control (MPC) strategy based on binary search algorithm is proposed to achieve the control purpose. The decoupling relationship between flying capacitor (FC) and output voltage is derived so that the proposed MPC strategy can control the voltage of two FCs simultaneously. In addition, the adoption of binary search algorithm effectively reduces the computation load of the proposed MPC strategy. Finally, the effectiveness of the proposed converter and MPC strategy are verified with a downscaled ESS experimental platform.**

***Index Terms*—Bidirectional four quadrant, energy storage system (ESS), flying capacitor (FC) dc/dc converter, model predictive control (MPC) strategy.**

I. INTRODUCTION

WITH the rapid development of power electronics, renewable energy represented by photovoltaic (PV) and wind power will become the dominated energy in the future [1], [2]. Energy storage technology, as the effective solution to solve the power fluctuation in microigrid, has drawn a lot of attention in recent years, and the electrochemical energy storage system (ESS) constructed by lithium battery has been used in many applications [3], [4].

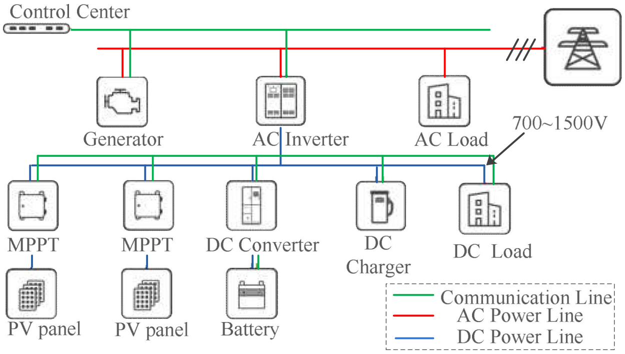

Fig. 1. Microgrid based on ESS on dc side.

Fig. 1 shows the grid structure with PV as the generation, in which ESS is placed at the dc side [5]. The energy generated by PV is aggregated into dc bus and fed into ac grid centrally through the grid-connected inverter. ESS in the microgrid is used to control the energy on dc bus according to PV generation and load conditions, suppress power fluctuations, and ensure the stability of ac grid, so bidirectional dc/dc converter is the key equipment in ESS. In order to improve system efficiency, nonisolated converter is often adopted, and three-level topology is the commonly used one [6], [7]. Compared with the two-level half bridge converter, three-level topology can reduce switch voltage stress by half, and the current ripple frequency can be doubled without changing switching frequency, helping to reduce the volume of filters. Currently, the nonisolated three-level topology mainly includes neutral point clamp (NPC) type and flying capacitor (FC) type [8], [9]. The NPC topology is composed of two half bridge converters in series. The basic principle and control scheme was studied in [10]. Actually, the NPC topology is similar to the half bridge converter in system control, however since the input and output ground of the converter is not common, NPC topology is difficult to operate in parallel. FC dc/dc converter realizes three-level operation through the parallel capacitor in the midpoint of upper and lower arms, and

Manuscript received August 29, 2021; revised December 11, 2021; accepted January 22, 2022. Date of publication January 27, 2022; date of current version March 24, 2022. This work was supported in part by the Natural Science Foundation of Jiangsu Province under Grant BK20200623, in part by the Natural Science Foundation of China under Grant 51807079, in part by the Postdoctoral Science Foundation of China under Grant 2020M681692, and in part by the Six Talent Peaks Project in Jiangsu Province GDZB-138. Recommended for publication by Associate Editor M. Ferdowsi. *(Corresponding author: Qigao Fan.)*

Kaitao Bi is with Jiangnan University, Wuxi 214122, China (e-mail: 1039451556@qq.com).

Huayang Lv and Liang Chen are with the College of Internet of Things Engineering, Jiangnan University, Wuxi 214122, China (e-mail: 16670123683@163.com; cl15256646199@163.com).

Jianfei Li is with the Sineng Electric Company, Ltd., Wuxi 214174, China (e-mail: lijianfei@si-neng.com).

Yixin Zhu, Wentao Huang, and Qigao Fan are with the School of Internet of Things Engineering, Jiangnan University, Wuxi 214122, China (e-mail: zhuyixin1987@163.com; wentao.h@jiangnan.edu.cn; qgfan@jiangnan.edu.cn).

Color versions of one or more figures in this article are available at https://doi.org/10.1109/TPEL.2022.3146510.

Digital Object Identifier 10.1109/TPEL.2022.3146510

the common ground structure is beneficial to expand system capacity in parallel [11], [12]. In contrast, the FC topology has obvious advantages applied in ESS.

However, the commonly studied FC dc/dc converter only works in two quadrant, which means that the converter can only work in buck or boost mode when energy is transmitted in one direction. As the microgrid shown in Fig. 1, since the power generation is PV, both the voltage on dc bus and energy storage side will have a wide changing range. At this time, the dc/dc converter shall have bidirectional four quadrant energy transmission capacity to meet the wide voltage variation condition on both sides. Callegaro *et al.* [13], [14] studied the two-level bidirectional four quadrant dc/dc converter applied in the PV system. On this basis, an interleaved modulation strategy with optimized phase shifting is proposed in [15] to decease inductor ripple current. However, the above research is only carried out for the two-level topology. Facing the application demand of higher voltage in ESS, it is necessary to expand the research to three-level bidirectional four quadrant FC topology.

In order to make the FC converter work reliably with three voltage level, the FC voltage should be controlled to half of the port voltage [9]. However, the differences in hardware parameters and system control will lead to FC voltage deviation, resulting in uneven voltage stress on switching devices. [16] and [17] studied the self-balancing property of FC converter and stated that the adverse effect of disturbance on the FC capacitor voltage can be offset in the circuit, as long as the disturbance is very small. However, the sources of disturbance have not been extensively investigated and the derived results are not common. The FC voltage control method based on *RLC* circuit is proposed in [18] and [19], which has acceptable reliability. However, the auxiliary circuit weakens system reliability and increases system cost. In addition, the phase disposition pulsewidth modulation (PD-PWM) and phase-shifted pulsewidth modulation (PS-PWM) methods are proposed in [20]–[24]. PS-PWM can achieve self-voltage control without auxiliary control methods, yet the voltage control performance is determined by switching frequency. In contrast, PD-PWM scheme has better control performance, but its implementation is much more complex. Model predictive control (MPC) is an attractive control strategy because of its inherent speed and simplicity. In recent years, MPC strategy has been extensively studied for dc–dc topologies [25]–[28]. However, the control performance depends on the converter model and predictive data. Therefore, understanding the control law between the predictive algorithm and FC voltage is crucial to the implementation of MPC in the FC dc/dc converter.

In order to meet the application requirements of ESS under the wide voltage conditions, this article proposes a FC bidirectional buck–boost converter, which has the ability to operate in bidirectional four quadrant. The proposed FCBBC consists of two FC arms and has an H-type topology. In Addition, based on the converter model, the predictive control law between bidirectional power control and FC voltage control is studied and a fixed frequency MPC strategy for the proposed converter applied in ESS is proposed. The control strategy can realize the system power and double FC voltage control at the same time. The salient contributions of this article are as follows.

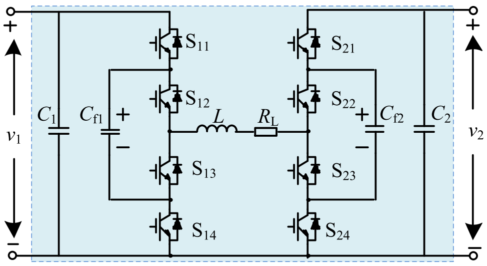

Fig. 2. Topology of FCBBC.

1) Proposing a FC dc/dc topology with bidirectional four quadrant operation capacity.
2) Detailed operation principle of FCBBC has been studied and presented.
3) Proposing a fixed frequency MPC strategy with the ability to achieve the decoupling control between dc bus voltage and double FC voltage.
4) Proposing an MPC optimization scheme based on binary search algorithm for FCBBC, helping to effectively reduce the computing load.

The rest of this article is organized as follows. Section II presents the basic principle of the proposed converter. Section III studies the converter model and proposes the MPC strategy, solving the bidirectional power and double FC control issues. The experimental results to verify the effectiveness of the proposed converter and MPC strategy are presented in Section IV. Finally, Section V concludes this article.

II. FC Bidirectional Buck–Boost DC/DC Converter

The topology of proposed FCBBC is shown in Fig. 2, with a symmetrical H-structure. Two FC arms are located in the input side and output side, respectively, and the two arms are connected through inductor L. C_{f1} and C_{f2} represent the FCs. R_L is the equivalent resistance of L. v_1 and v_2 are used to describe the input and output voltages of the converter, respectively.

In order to make FCBBC operate with three voltage level, the drive signals of S_{11} and S_{14}, S_{12}, and S_{13} are complementary, and S_{11} and S_{12} has the same duty ratio, but their carrier shifts 180 °. Similarly, S_{21}–S_{24} have the same driving principle. Because of the symmetrical structure, FCBBC has buck, boost, and buck–boost three operation modes. Taking energy flowing from v_1 to v_2 as the example. When the converter operates in buck mode, S_{11} and S_{12} are turned ON by turns, other switches are closed, and the body diodes of S_{21} and S_{22} provide the energy flowing path. The circuit states are shown in Fig. 3.

When the FCBBC operates in the boost mode, S_{11} and S_{12} are turned ON continuously, S_{23} and S_{24} conduct by turns, and other switches are turned OFF. Thus, the circuit states are shown in Fig. 4.

The driving principle in buck–boost mode are relatively complex. S_{11} and S_{12} operate complementary, S_{23} and S_{24} operate

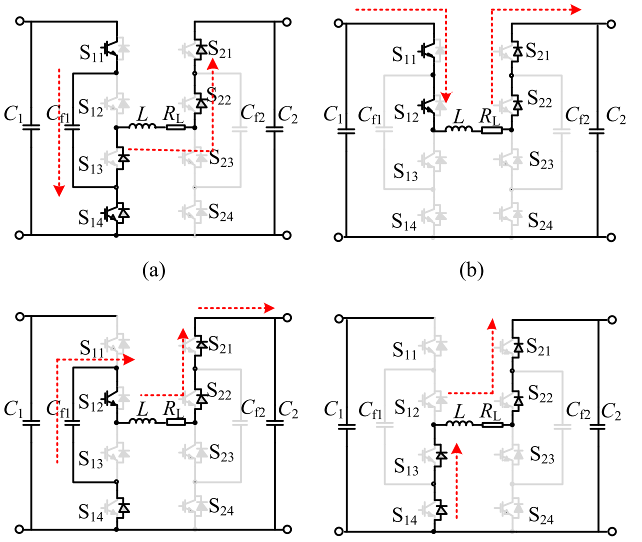

(a) (b) (c) (d)

Fig. 3. Operating states under buck mode. (a) State one. (b) State two. (c) State three. (d) State four.

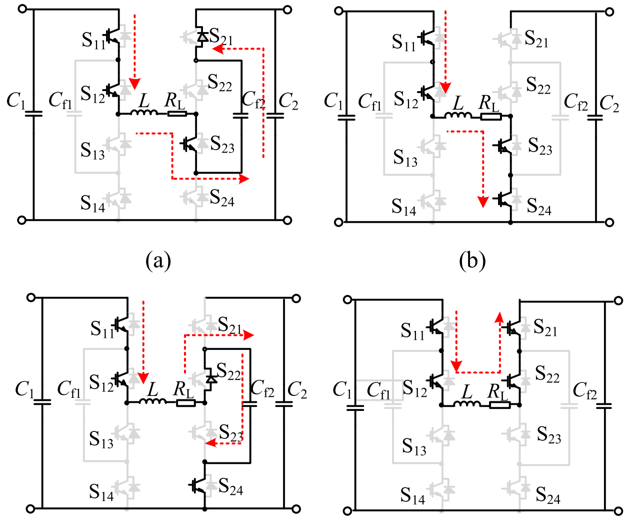

(a) (b) (c) (d)

Fig. 4. Operating states under boost mode. (a) State one. (b) State two. (c) State three. (d) State four.

complementary, and the carriers of S_{11} and S_{24} are the same. At this time, the circuit states are shown in Fig. 5.

Because of the symmetrical structure, the overall operating mode of FCBBC can be shown in Fig. 6. It can be seen that FCBBC can work with buck and boost modes during bidirectional energy conversion, so it has bidirectional four quadrant energy transmission capability.

As shown in Figs. 3–5 that there are four states for FCBBC in each operation mode. The definite operating states in each switching period are determined by the duty ratio, and the telling rules are given in Table I, where d_{11} and d_{24} represent the duty ratios of S_{11} and S_{24}, respectively.

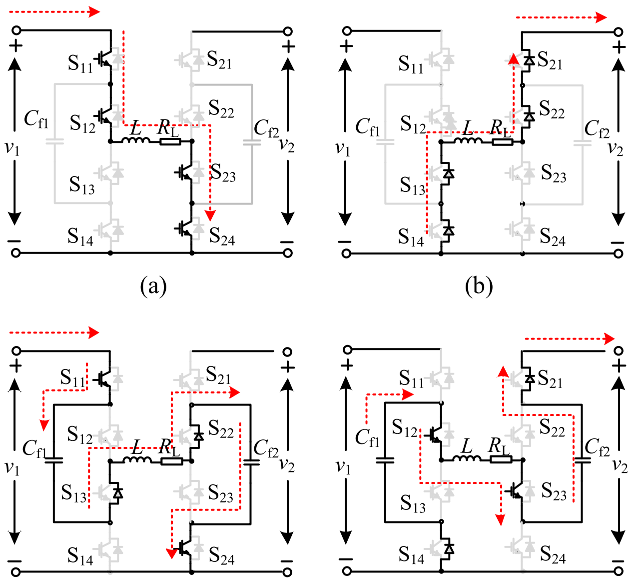

(a) (b) (c) (d)

Fig. 5. Operating states under buck-boost mode. (a) State one. (b) State two. (c) State three. (d) State four.

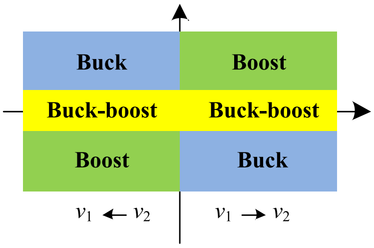

Fig. 6. Operation modes of FCBBC with bidirectional four quadrant.

TABLE I
OPERATING STATES OF FCBBC UNDER DIFFERENT DUTY RATIOS

Operation mode	Duty ratio	Operation state
Buck	d_{11}<0.5, d_{24}=0	Fig.3(a), Fig.3(c), Fig.3(d)
Buck	d_{11}>0.5, d_{24}=0	Fig.3(a), Fig.3(b), Fig.3(c)
Buck	d_{11}=0.5, d_{24}=0	Fig.3(a), Fig.3(c)
Boost	d_{11}=1, d_{24}>0.5	Fig.4(a), Fig.4(b), Fig.4(c)
Boost	d_{11}=1, d_{24}<0.5	Fig.4(a), Fig.4(c), Fig.4(d)
Boost	d_{11}=1, d_{24}=0.5	Fig.4(a), Fig.4(c)
Buck-Boost	(d_{11}= d_{24})>0.5	Fig.5(a), Fig.5(c), Fig.5(d)
Buck-Boost	(d_{11}= d_{24})<0.5	Fig.5(b), Fig.5(c), Fig.5(d)
Buck-Boost	(d_{11}= d_{24})=0.5	Fig.5(c), Fig.5(d)

According to Fig. 5 and Table I, the driving signals and current ripple waveform in buck–boost mode can derived, which is shown in Fig. 7.

As can be seen from Fig. 7, except that the duty ratio is 0.5, the current ripple frequency is twice of switching frequency. Thus,

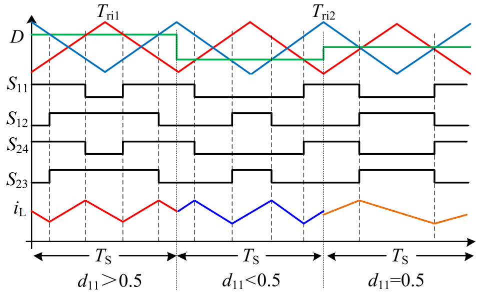

Fig. 7. Driving signals and current ripple under buck–boost mode.

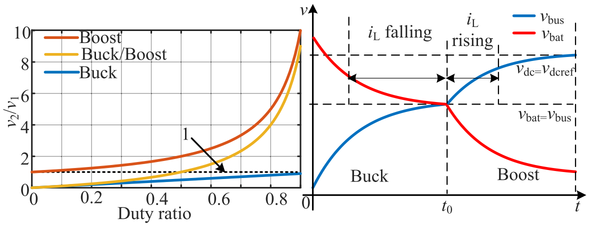

(a) (b)

Fig. 8. Operation characteristics of FCBBC. (a) Voltage gain. (b) Mode switching from Buck mode to Boost.

FCBBC can always be controlled to work under three-level with such driving principle.

According to the circuit state equation shown in Appendix and Table I, the voltage gain of the FCBBC can be derived, as shown in (1), and the detailed derivation process of (1) is presented in the Appendix

$$\begin{cases} v_2 = d_{11} \cdot v_1 & \text{Buck} \\ v_2 = \frac{1}{1-d_{24}} \cdot v_1 & \text{Boost} \\ \\ v_2 = \frac{d_{11}}{1-d_{11}} \cdot v_1 & \text{Buck-boost.} \end{cases} \tag{1}$$

Actually, the voltage gain of FCBBC shown in (1) is basically the same as that of the traditional FC dc/dc converter, so the hardware parameter design principle of FCBBC can refer to the traditional one [29]. Thus, the inductor and FC design rules are expressed as

$$\begin{cases} L_{\min} = \frac{v_1}{2\Delta I_{L\max} f_s} \\ C_{f\min} = \frac{I_L}{2\Delta v_{\text{flymax}} f_s} \end{cases} \tag{2}$$

where $\triangle I_{L\max}$ is the maximum current ripple, f_s is the switching frequency, $\triangle V_{\text{flymax}}$ is the maximum voltage ripple of FC. The detailed derivation of (2) is shown in the Appendix.

According to (1), we can have the voltage gain curves of FCBBC in three modes, as shown in Fig. 8(a). It can be seen that the mode switching between buck and boost is discontinuous. Taking discharge operation as an example, when the operation mode of FCBBC is changed from buck to boost, it is necessary to ensure that the voltage at energy storage side is less than or equal to the dc bus voltage for the control of system current. However, when the voltage difference between dc bus and energy storage side is small, the current response will be slow, which will affect the system response speed. The detailed response curves are shown in Fig. 8(b).

In contrast, as shown in Fig. 8(a), the voltage gain curve of FCBBC in the buck–boost mode is continuous, which means that the mode switching will not be affected by the voltage difference on the converter input and output side. Therefore, the converter will have favorable response performance under a wide range of voltage range. So, the FCBBC is more suitable to work with buck–boost mode in the ESS. The following research on control strategy mainly focuses on the buck–boost mode.

III. MPC STRATEGY FOR FCBBC

The following control requirements have to be considered when designing the MPC strategy for FCBBC applied in ESS.

1) Having the ability to achieve bidirectional power conversation and stabilize the dc bus voltage.
2) Having the ability to control the dual FCs voltage.
3) Having favorable dynamic response to meet the rapid response requirements of ESS.

Based on these requirements, an improved fixed frequency MPC strategy is proposed in this section. First, the model of FCBBC is analyzed.

A. *Mathematical Model of FCBBC*

As shown in Fig. 5(a), S_{11}, S_{12}, S_{24}, and S_{23} are turned ON simultaneously, and there are no charge or discharge circuits for C_{f1} and C_{f2}. Thus, the state equation of Fig. 5(a) can be expressed as

$$\frac{d}{dt}\begin{bmatrix} i_L \\ v_{f1} \\ v_{f2} \end{bmatrix} = \begin{bmatrix} -\frac{R_L}{L} & 0 & 0 \\ 0 & 0 & 0 \\ 0 & 0 & 0 \end{bmatrix} \begin{bmatrix} i_L \\ v_{f1} \\ v_{f2} \end{bmatrix} + \begin{bmatrix} \frac{1}{L} & 0 \\ 0 & 0 \\ 0 & 0 \end{bmatrix} \begin{bmatrix} v1 \\ v2 \end{bmatrix}. \tag{3}$$

In Fig. 5(b), S_{11}, S_{12}, $S_{24,}$ and S_{23} are turned OFF. And there are also no charge or discharge circuits for C_{f1} and C_{f2}. The state equation of Fig. 5(b) is expressed as

$$\frac{d}{dt}\begin{bmatrix} i_L \\ v_{f1} \\ v_{f2} \end{bmatrix} = \begin{bmatrix} -\frac{R_L}{L} & 0 & 0 \\ 0 & 0 & 0 \\ 0 & 0 & 0 \end{bmatrix} \begin{bmatrix} i_L \\ v_{f1} \\ v_{f2} \end{bmatrix} + \begin{bmatrix} 0 & -\frac{1}{L} \\ 0 & 0 \\ 0 & 0 \end{bmatrix} \begin{bmatrix} v1 \\ v2 \end{bmatrix}. \tag{4}$$

As shown in Fig. 5(c), S_{11} and S_{24} are turned ON, S_{12} and S_{23} are turned OFF, and C_{f1} and C_{f2} are charged by system current. At this time, the state equation is written as

$$\frac{d}{dt}\begin{bmatrix} i_L \\ v_{\text{f1}} \\ v_{\text{f2}} \end{bmatrix} = \begin{bmatrix} -\frac{R_L}{L} & -\frac{1}{L} & -\frac{1}{L} \\ \frac{1}{C_{f1}} & 0 & 0 \\ \frac{1}{C_{f2}} & 0 & 0 \end{bmatrix} \begin{bmatrix} i_L \\ v_{f1} \\ v_{f2} \end{bmatrix} + \begin{bmatrix} \frac{1}{L} & 0 \\ 0 & 0 \\ 0 & 0 \end{bmatrix} \begin{bmatrix} v1 \\ v2 \end{bmatrix}. \tag{5}$$

S_{11} and S_{24} are turned OFF in Fig. 5(d), S_{12} and S_{23} are turned ON. The energy stored in C_{f1} and C_{f2} is released. The state equation is expressed as

$$\frac{d}{dt}\begin{bmatrix} i_L \\ v_{f1} \\ v_{f2} \end{bmatrix} = \begin{bmatrix} -\frac{R_L}{L} & \frac{1}{L} & \frac{1}{L} \\ -\frac{1}{C_{f1}} & 0 & 0 \\ -\frac{1}{C_{f2}} & 0 & 0 \end{bmatrix} \begin{bmatrix} i_L \\ v_{f1} \\ v_{f2} \end{bmatrix} + \begin{bmatrix} 0 & -\frac{1}{L} \\ 0 & 0 \\ 0 & 0 \end{bmatrix} \begin{bmatrix} v1 \\ v2 \end{bmatrix}. \tag{6}$$

When the FCBBC operates under steady state, the voltage of the two FCs should be equal to half of the port voltage on their respective sides to ensure the stable operation, thus we can have

$$\begin{cases} v_{f1} = \frac{1}{2}v1 \\ v_{f2} = \frac{1}{2}v2 \end{cases}. \tag{7}$$

Substituting (7) into (5) and (6), respectively. The modified (5) and (6) are shown in

$$\frac{d}{dt}\begin{bmatrix} i_L \\ v_{f1} \\ v_{f2} \end{bmatrix} = \begin{bmatrix} -\frac{R_L}{L} & 0 & 0 \\ \frac{1}{C_{f1}} & 0 & 0 \\ \frac{1}{C_{f2}} & 0 & 0 \end{bmatrix}\begin{bmatrix} i_L \\ v_{f1} \\ v_{f2} \end{bmatrix} + \begin{bmatrix} \frac{1}{2L} & -\frac{1}{2L} \\ 0 & 0 \\ 0 & 0 \end{bmatrix}\begin{bmatrix} v1 \\ v2 \end{bmatrix} \tag{8}$$

$$\frac{d}{dt}\begin{bmatrix} i_L \\ v_{f1} \\ v_{f2} \end{bmatrix} = \begin{bmatrix} -\frac{R_L}{L} & 0 & 0 \\ -\frac{1}{C_{f1}} & 0 & 0 \\ -\frac{1}{C_{f2}} & 0 & 0 \end{bmatrix}\begin{bmatrix} i_L \\ v_{f1} \\ v_{f2} \end{bmatrix} + \begin{bmatrix} \frac{1}{2L} & -\frac{1}{2L} \\ 0 & 0 \\ 0 & 0 \end{bmatrix}\begin{bmatrix} v1 \\ v2 \end{bmatrix}. \tag{9}$$

Assuming d_{12} and d_{23} as the duty ratio of S_{12} and S_{23}, respectively. According the operation states given in Table I and (3), (4), (8), and (9), the equivalent steady-state equation of FCBBC can be derived as

$$\frac{d}{dt}\begin{bmatrix} i_L \\ v_{f1} \\ v_{f2} \end{bmatrix} = \begin{bmatrix} -\frac{R_L}{L} & 0 & 0 \\ \frac{d11-d12}{C_{f1}} & 0 & 0 \\ \frac{d24-d23}{C_{f2}} & 0 & 0 \end{bmatrix}\begin{bmatrix} i_L \\ v_{f1} \\ v_{f2} \end{bmatrix} + \begin{bmatrix} \frac{d11+d12}{2L} & \frac{d11+d12-2}{2L} \\ 0 & 0 \\ 0 & 0 \end{bmatrix}\begin{bmatrix} v1 \\ v2 \end{bmatrix}. \tag{10}$$

Generally speaking, dc bus voltage, inductance current and the two FCs voltage must to be controlled when FCBBC applied in ESS. Taking the inductance current and FC voltage as the internal control variables, it can be seen from (10) that the current control depends on the port voltage difference and the duty ratio of S_{11} and S_{12}, and the FC voltage control depends on the inductance current and duty ratio difference on the upper arm. These relationships show that current control is the premise for the converter to achieve normal operation. In other words, when the current control is achieved, the voltage control of FC will be obtained naturally.

B. MPC Strategy Design

To design the MPC strategy, the FC voltage and system current is treated as the control variables. Equation (10) is discretized with Euler discretization method, and the discretized equation is shown as follows:

$$\begin{cases} i_L^{k+1} = (1 + \frac{T_s R_L}{L})i_{\mathrm{L}}^k + \frac{T_s}{2L}((d_{11} + d_{12})v_1^k \\ +(d_{11} + d_{12} - 2)v_2^k) \\ v_{f1}^{k+1} = v_{\mathrm{f1}}^k + \frac{T_s}{C_{f1}}(d_{11} - d_{12})i_L^k \\ v_{f2}^{k+1} = v_{f2}^k + \frac{T_s}{C_{f2}}(d_{24} - d_{23})i_L^k \end{cases} \tag{11}$$

where T_{s} is the switching period, the symbol marked with k is the sampling value at current time, and the symbol with k+1 is the predicted value for the next period.

The cost function in the traditional MPC algorithm can be obtained by (11), which is expressed as

$$J^k = \lambda 1(i_L^* - i_L^{k+1})^2 + \lambda 2(v_{f1}^* - v_{f1}^{k+1})^2 + \lambda 3(v_{f2}^* - v_{f2}^{k+1})^2 \tag{12}$$

where the symbols marked with $*$ are the reference variables, λ_1, λ_2, and λ_3 are the weight factors of system current and FC voltage, respectively.

It can be seen from (11) that the traditional MPC algorithm should consider all the possible combinations of d_{11}, d_{12}, d_{24}, and d_{23} to get the optimal control performance, which brings a heavy computational burden for the controller. Second, multiple weight factors have to be designed as shown in (12). However, it is hard to design the weight factors because there is no standard design rules at present. Third, the prediction of switching state is often used in power electronic control, which is easy to cause the switch to operate in variable frequency, increasing power loss.

To solve the above issues, the duty ratio in (11) is rewritten as

$$\begin{cases} g_L = \frac{d11+d12}{2} = \frac{d24+d23}{2} & 0 \le g_L \le 1 \\ g_{f1} = \frac{d11-d12}{2} & -0.5 \le g_{f1} \le 0.5 \\ g_{f2} = \frac{d24-d23}{2} & -0.5 \le g_{f2} \le 0.5 \end{cases}. \tag{13}$$

Substituting (13) into (11), we can have

$$\begin{cases} i_L^{k+1} = (1 + \frac{T_s R_L}{L})i_L^k + \frac{T_s}{L}(g_L v_1^k + (g_L - 1)v_2^k) \\ v_{f1}^{k+1} = v_{f1}^k + 2\frac{T_s}{C_{f1}}g_{f1}i_L^k \\ v_{f2}^{k+1} = v_{f2}^k + 2\frac{T_s}{C_{f2}}g_{f2}i_L^k \end{cases}. \tag{14}$$

As shown in (14), the system current and FC voltage can be predicted through duty ratios. In addition, the most important is that there is no coupling relationship between the three predictive variables, which means that i_L^{k+1}, v_{f1}^{k+1}, and v_{f2}^{k+1} are decoupled. Thus, the cost function can be designed as

$$\begin{cases} J_L^k = (i_L^* - i_L^{k+1})^2 \\ J_{f1}^k = (v_{f1}^* - v_{f1}^{k+1})^2 \\ J_{f2}^k = (v_{f2}^* - v_{f2}^{k+1})^2 \end{cases} \tag{15}$$

where ${J_L}^k$, ${J_{f1}}^k$, and ${J_{f2}}^k$ are the cost function of system current and the two FCs, respectively.

It can be known form (15) that it is feasible to build independent closed-loops to control system current and FC voltage. At the same time, the weight factors are eliminated and all the switches can operate with a fixed switching frequency. However, it has to be admitted that the higher accuracy of predicting the duty ratio helps to get better control performance, but it will result a larger computation load. In order to improve computing efficiency, the binary search algorithm is adopted in this article to optimize the duty ratio search.

The basic principle of binary search is to compare the target element with the element in the middle of the linear sequence, thus the regional position of the target element can be obtained. Then with recursion in turn, the optimal solution can be found. As shown in (14), each variable has a linear relationship with the duty ratio, so the regional position of the target value can be obtained according to the difference between the target value and the predicted value. So, assuming $B_{x(i)}$ and $T_{x(i)}$ represent the bottom and top boundary of duty ratio for the ith computing interval in one switching period, respectively. The subscript x indicates the three symbols: L; f_1; and f_2. Thus, the equations to select $g_{L(i)}$, $g_{f1(i)}$, and $g_{f2(i)}$ according to the binary search algorithm can be expressed as

$$\begin{cases} g_{L(i)} = \frac{B_{L(i)}+T_{L(i)}}{2} \\ g_{f1(i)} = \frac{B_{f1(i)}+T_{f1(i)}}{2} \\ g_{f2(i)} = \frac{B_{f2(i)}+T_{f2(i)}}{2} \end{cases}. \tag{16}$$

The preliminarily duty ratio can be derived using the boundary value based on (16). Substituting the obtained duty ratio into (14), we can have the predicted values. Then, the difference between the predicted value and the reference value is derived according to

$$\begin{cases} P_{L(i)} = i_{L(i)}^{k+1} - i_L^* \\ P_{f1(i)} = v_{f1(i)}^{k+1} - v_{f1}^* \\ P_{f2(i)} = v_{f2(i)}^{k+1} - v_{f2}^* \end{cases}. \tag{17}$$

The difference values derived in (16) are used to update the boundary $B_{x(i)}$ and $T_{x(i)}$ for the next computational interval, as shown in

$$\begin{cases} B_{x(i+1)} = g_{x(i)} \ \text{if}(P_{x(i)} \geq 0) \\ T_{x(i+1)} = g_{x(i)} \ \text{if}(P_{x(i)} < 0) \end{cases}. \tag{18}$$

Repeat the operations expressed by (16)–(18) successively until the optimal variables satisfying the cost function. Thus, we can get the optimal duty ratios g_L, $g_{f1,}$ and g_{f2}, and then transform g_L, g_{f1}, and g_{f2} using the equation shown in (19), the expression of the final output duty ratios can be obtained

$$\begin{cases} d_{11} = g_L + g_{f1} \\ d_{12} = g_L - g_{f1} \\ d_{24} = g_L + g_{f2} \\ d_{23} = g_L - g_{f2} \end{cases}. \tag{19}$$

Since the main function of ESS is to control dc bus voltage, output voltage control must be added in the proposed MPC strategy.

According to the operating principle of the converter in ESS, the relationship between system current and output voltage can be expressed as

$$\begin{aligned} v_2 &= i_L(1 - D_{\text{st}})R_2 \\ &= i_2 R_2 \end{aligned} \tag{20}$$

where R_2 is the load resistance, D_{st} is the equivalent steady-state duty ratio, and i_2 is the load current.

The current reference can be derived based on (1) and (20), which is shown as follows:

$$i_L^* = \frac{v_2^*(v_2^* + v_1^k)}{v_1^k R_2}. \tag{21}$$

As shown in (21), the current reference is determined by R_2, which means that the load current is inevitable to estimate R_2. Thus, the expression of i_L^* can be rewritten as follows:

$$i_L^* = \frac{v_2^*(v_2^* + v_1^k)v_2^k}{v_1^k i_2^k}. \tag{22}$$

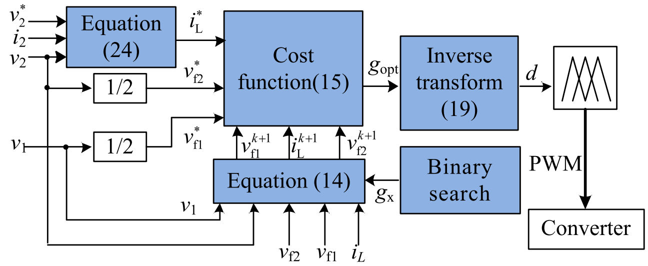

Fig. 9. Schematic of the proposed MPC strategy for FCBBC.

As mentioned earlier, the two FC voltage should be controlled to half of the voltage on each side to ensure that the converter operates in three-level mode. Therefore, the voltage reference of the FC voltage can be obtained by direct sampling of the voltages on both sides, which can be expressed as

$$\begin{cases} v_{f1}^* = \frac{v_1^k}{2} \\ v_{f2}^* = \frac{v_2^k}{2} \end{cases}. \tag{23}$$

Thus, the final MPC strategy can be obtained by combining the equations from (14) to (23), and the control block diagram is shown in Fig. 9.

The MPC strategy predicts the optimal control variables using the current sampling information, different duty ratios and reference values. All the predicted values are filtered by the cost function, and the optimal variable g_{opt}, which minimizes the cost function, is selected as the output control variable. The duty ratio for each switch is derived through the inverse transformation of g_{opt}, and then the PWM driving signal is obtained. The detailed flow chart of the proposed MPC strategy based on binary search algorithm is shown in Fig. 10.

C. Calculation Efficiency Analysis of the Proposed MPC Strategy

Considering the four duty ratios in (11), the optimiza-tion calculation times of traditional MPC strategy in one switching period can be expressed as

$$C_t = \left(\frac{1}{\Delta g} + 1\right)^4 \tag{24}$$

where Δg is the duty ratio division precision.

According the binary search algorithm, the optimization calculation times of the proposed MPC strategy is

$$C_n = \text{ceil}\left(\log_2\left(\frac{1}{\Delta g} + 1\right)\right) \tag{25}$$

where ceil () is the upward rounding function.

Thus, the computation comparison diagram between the traditional MPC strategy and the proposed MPC can be derived based on (24) and (25), as shown in Fig. 11. Compared with the traditional method, the proposed MPC strategy significantly reduces the computational burden, helps to reduce the requirements for the controller, and is easier to be applied in practice.

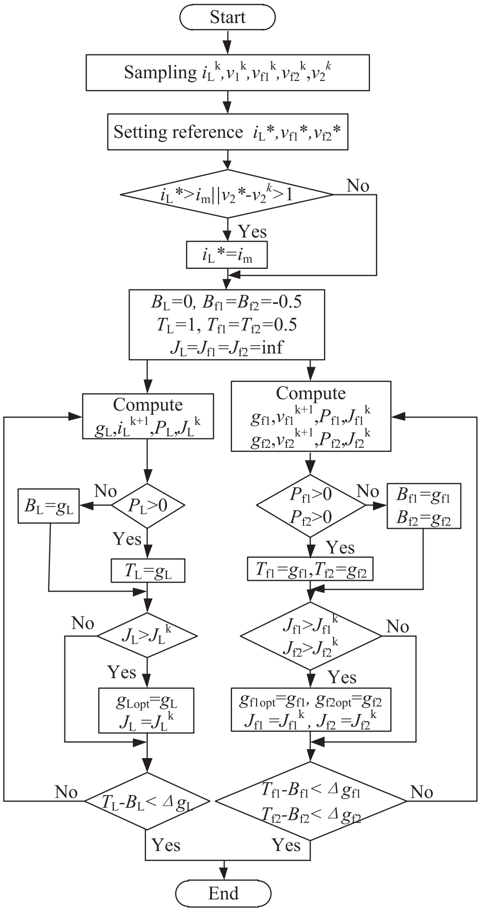

Fig. 10. Flow chart of the proposed MPC strategy.

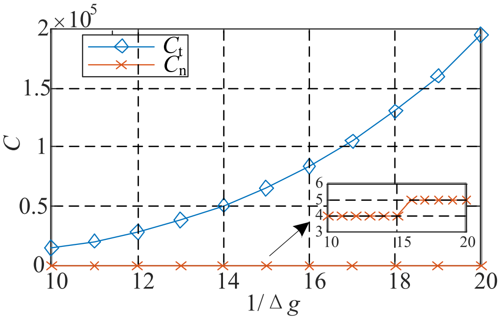

Fig. 11. Relationship between calculation times with duty ratio sampling precision.

D. Stability Analysis

The stability of the control strategy is important for the reliable operation of the system. Direct Lyapunov method is used in this article to proof the stability of the proposed MPC strategy. The direct Lyapunov method of stability shows that if a positive definite Lyapunov function $L(x)$ related to the system states x exists, the stability of the system can be ensured if the following conditions can be satisfied.

1) $L(x)$ is a positive definite.
2) $\dot{L}(x)$ is a negative definite.
3) $L(x)$ tends to ∞ if $\|x\| \to \infty$.

Lyapunov function can be treated as an "energy-like" function. The increase in the function means the increase of state norm, and the decrease of function means the decrease of state norm. When $L(x)$ is zero, the state is stable at the origin $x = 0$ [30].

According to the cost function shown in (15), the discrete Lyapunov function is written as

$$L(\mathbf{x})^k = \frac{1}{2}\left[\mathbf{x}_{L\_\mathrm{err}}^{k+1}\right]^{\mathrm{T}}\left[\mathbf{x}_{L\_\mathrm{err}}^{k+1}\right] \tag{26}$$

where $\mathbf{x}$ can be expressed as $[i_L\ v_{f1}\ v_{f2}]^T$.

According to the MPC prediction results, the system current and FC voltage errors are defined as follows:

$$\begin{cases} i_{L\_\mathrm{err}}^{k+1} = i_L^{k+1} - i_L^* \\ v_{f1\_\mathrm{err}}^{k+1} = v_{f1}^{k+1} - v_{f1}^* \\ v_{f2\_\mathrm{err}}^{k+1} = v_{f2}^{k+1} - v_{f2}^* \end{cases}. \tag{27}$$

The change rate of Lyapunov function of system current and FC voltage can be derived based on (26) and (27), which is shown as follows:

$$\begin{aligned} \Delta L(i_L)^k &= L(i_L)^{k+1} - L(i_L)^k \\ &= \frac{1}{2}\left[\left(1+\frac{T_sR_L}{L}\right)i_{\mathrm{L}}^k + \frac{T_s}{L}(g_Lv_1^k + (g_L-1)v_2^k) - i_L^*\right] \\ &\quad \times \left[\left(1+\frac{T_sR_L}{L}\right)i_L^k + \frac{T_s}{L}(g_Lv_1^k + (g_L-1)v_2^k) - i_L^*\right] \\ &\quad - \frac{1}{2}\left[i_{L\_\mathrm{err}}^k\right]\times\left[i_{L\_\mathrm{err}}^k\right] \end{aligned} \tag{28}$$

$$\begin{aligned} \Delta L(v_{fi})^k &= L(v_{fi})^{k+1} - L(v_{fi})^k \\ &= \frac{1}{2}\left[v_{fi}^k + 2\frac{T_s}{C_{fi}}g_{fi}i_L^k - v_{fi}^*\right] \\ &\quad \times \left[v_{fi}^k + 2\frac{T_s}{C_{fi}}g_{fi}i_L^k - v_{fi}^*\right] \\ &\quad - \frac{1}{2}\left[v_{fi\_err}^k\right]\times\left[v_{fi\_\mathrm{err}}^k\right] \end{aligned} \tag{29}$$

where i indicates ($i = 12$).

In order to make the tracking error converge to zero in the proposed MPC strategy, it is necessary to ensure that the change rate of Lyapunov function is always negative. Considering the tracking characteristics of MPC strategy, we can have following approximation according (14) and (15)

$$i_L^* \approx \left(1+\frac{T_sR_L}{L}\right)i_L^k + \frac{T_s}{L}(g_Lv_1^k + (g_L-1)v_2^k) \tag{30}$$

$$v_{fi}^* \approx v_{fi}^k + 2\frac{T_s}{C_{\mathrm{fi}}}g_{fi}i_L^k. \tag{31}$$

Substituting (30) and (31) into (28) and (29), respectively, the following equations can be derived:

$$\begin{cases} \Delta L(i_L)^k = -\frac{1}{2}(i_{L\_\mathrm{err}}^k)^2 \\ \Delta L(v_{fi})^k = -\frac{1}{2}(v_{fi\_\mathrm{err}}^k)^2 \end{cases}. \tag{32}$$

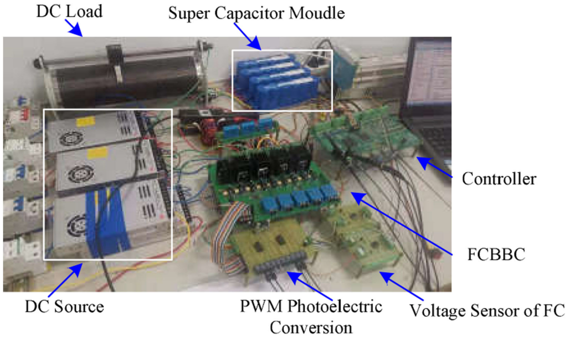

Fig. 12. Experimental platform.

TABLE II
EXPERIMENTAL PARAMETERS

Item	Value	Unit
Energy storage side voltage	24	V
Switching frequency	10k	Hz
System inductance	1.6	mH
Flying capacitor	220	μF
Filter capacitor	500	μF
Load adjustable resistor	4	Ω

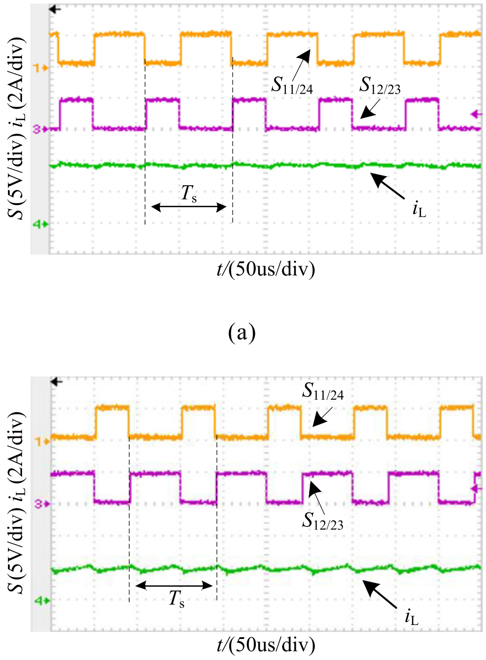

(a)

(b)

Fig. 13. Drive signals and current ripple. (a) Duty ratio larger than 0.5. (b) Duty ratio smaller than 0.5.

Thus, according to (26) and (32) and the determine principle of Lyapunov direct method, the stability of the proposed MPC strategy in this article can be ensured.

IV. EXPERIMENTAL VERIFICATION

In order to verify the effectiveness of the proposed FCBBC and MPC strategy, a downscaled energy storage experimental platform is built in the laboratory. The digital signal processor (DSP) TMS320F28335 and field programmable gate array (FPGA) XC3S500E are employed as the controller. DSP is responsible for sampling and data processing, and FPGA is used to generate driving signals and achieve protection. The platform picture is shown in Fig. 12. Supercapacitor module with the capacity of 9.6F/16V are adopted as the energy storage device. The dc sources in Fig. 12 are employed to precharge super capacitor modules and FCs to 24 V before the experiment based on the experimental settings. A power resistor is used at the grid side to simulate dc load. The detailed experimental parameters are given in Table II.

A. *Experimental Results*

The current ripple curves with different duty ratios are shown in Fig. 13. It can be seen that the ripple frequency is always two times of the switching frequency, which means that the FCBBC operates with three voltage level in the buck–boost mode.

The verification results for the FCBBC and MPC strategy are shown in Figs. 14 and 15. Fig. 14 shows the experimental results under buck operation. With the proposed MPC strategy, the initial output voltage is 12 V and then the output voltage reference steps to 20 V. The response curves of inductance current and output voltage are shown in Fig. 14(a). Since a digital filter is used in sampling processing, the inductance current and output voltage reach the steady state after a short oscillation. The FC voltage curves are shown in Fig. 14(b). Since the input voltage is 24 V, with the proposed MPC strategy, v_1 is always stable at 12 V and does not change, and v_2 follows the change of output voltage, increases from 6 to 10 V. When the output voltage reference is declined from 20 to 12 V, the experimental results are shown in Fig. 14(c) and (d). At this time, the output voltage of the converter still strictly tracks the reference, and also has favorable control ability of FC voltage.

Fig. 15 shows the experimental results in the buck–boost mode. Fig. 15(a) and (b) shows the response curves when the voltage reference steps from 20 to 30 V. In this period, the inductance current rises from 10 to 22 A after a short oscillation, and the output voltage finally stabilizes to 30 V, tracking the voltage reference.

The voltage response curves of FC are shown in Fig. 15(b). At this time, v_{f1} remains unchanged at 12V, and the voltage of v_{f2} rises from 10 to 15 V, which remains half of the output voltage. When the output voltage reference steps from 30 to 20 V, the response curves are shown in Fig. 15(c) and (d). At this time, the output voltage and FC voltage can still be well controlled.

The dynamic response results of the proposed FCBBC and MPC strategy are shown in Fig. 16. Fig. 16(a) shows the abruptly loaded response results. It can be seen from Fig. 16(a) that the output voltage v_2 drops by 2 V when another resistor is cut into the system and the FC voltage at output side fluctuates slightly. The fluctuation time of v_2 lasts about 4 ms and the final system current increases by 40%. The abruptly unloaded curves are shown in Fig. 16(b). At this moment, the resistor is cut OFF from

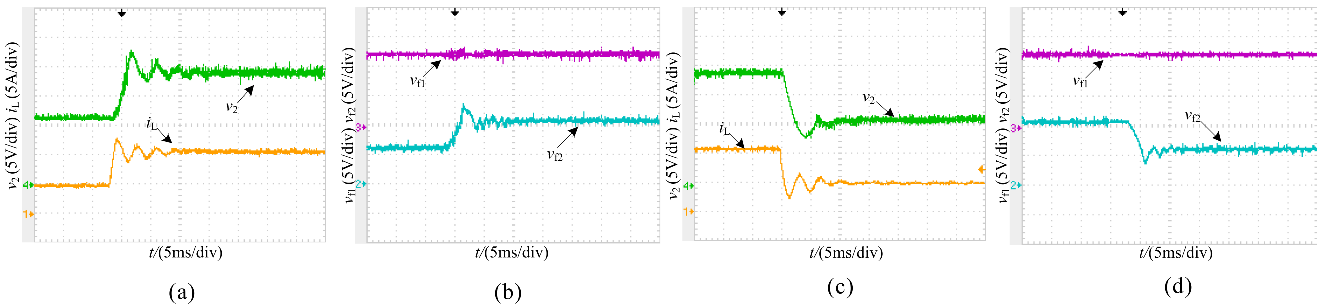

Fig. 14. Experimental results with buck operation. (a) Response curves of i_L and v_2 when the voltage reference increases. (b) FC voltage curves when the voltage reference increases. (c) Response curves of i_L and v_2 when the voltage reference declines. (d) FC voltage curves when the voltage reference declines.

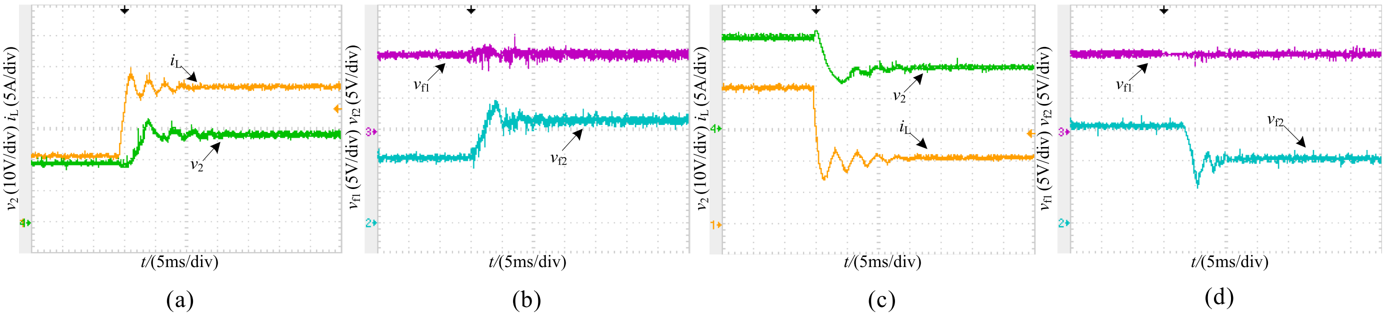

Fig. 15. Experimental results with buck–boost operation. (a) Response curves of i_L and v_2 when the voltage reference increases. (b) FC voltage curves when the voltage reference increases. (c) Response curves of i_L and v_2 when the voltage reference declines. (d) FC voltage curves when the voltage reference declines.

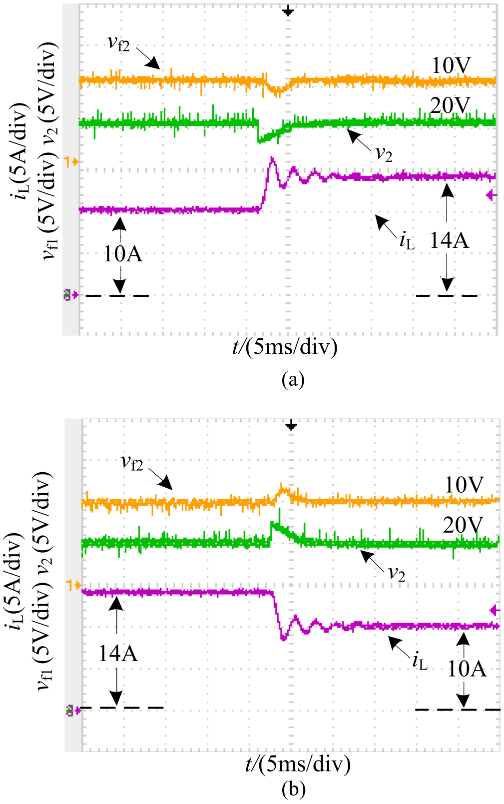

Fig. 16. Dynamic response results. (a) Load increasing. (b) Load decreasing.

the system. It can be seen that the voltage of v_2 rises briefly, and returns to normal after 4 ms. The system current is stabilized to 10A after a short fluctuation. According to the curves shown in Fig. 16, we can know that the proposed FCBBC and MPC strategy have good control performance in case of abruptly load change.

According to the above results, the FCBBC can transmit energy with buck and boost operation from v_1 to v_2. Due to the symmetrical structure, when the energy flows in the opposite direction, the FCBBC has the same power conversion capability. So, the FCBBC can operate in bidirectional four quadrant. At the same time, the proposed MPC strategy can achieve favorable voltage control performance, including output voltage, and dual FC voltages. Therefore, the proposed model predictive controlled FCBBC is suitable for the application of ESS in the wide dc bus voltage range condition.

B. Comparison With Other Topologies

In order to highlight the characteristics of FCBBC, two bidirectional four quadrant topologies are selected for comparative analysis, which are shown in Fig. 17. The two-level topology is shown in Fig. 17(a), which has an H-bridge structure to realize power bidirectional four quadrant operation. Fig. 17(b) shows the currently used three-level bidirectional four quadrant topology in industry, which is evolved from the neutral point clamped three-level topology.

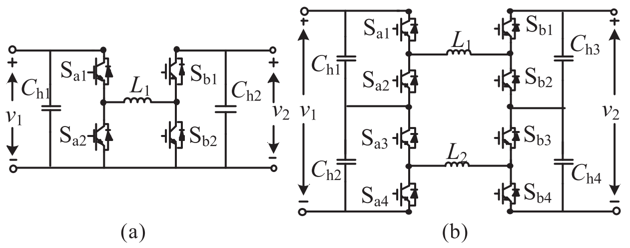

Fig. 17. Traditional bidirectional four quadrant dc/dc topology. (a) Two level [14], [15]. (b) Three level [31].

Both of the two topologies in Fig. 17 have three operating modes: buck; boost; and buck–boost. Due to the voltage stress of switching device, the two-level topology in Fig. 17(a) is hard to be applied in high-voltage occasions, and the two-level topology requires larger filters under the same working conditions. The three-level topology shown in Fig. 17(b) has the same driving principle with FCBBC. The voltage level of switching device and filter elements are almost the same. The main difference between FCBBC and the topology shown in Fig. 17(b) are as follows.

1) Compared with FCBBC, the input and output ground of the three-level topology shown in Fig. 17(b) is not common, so FCBBC is easy to work in parallel and is more suitable for the high-power occasions.
2) The control of FCBBC is relatively difficult. First, it is necessary to solve the precharging issue of FC, and secondly, the FC voltage has to be balanced during operation.

In contrast, FCBBC is more suitable for the high-power occasions with multiple converters in parallel, while the topology shown in Fig. 17(b) is suitable for the low-power occasions.

For the efficiency of the two topologies, since the driving principle is the same, FCBBC and the topology shown in Fig. 17(b) have the same switching loss. So, only the efficiency of FCBBC is analyzed in the following article.

The switching device loss includes insulated gate bipolar transistor (IGBT) loss and body diode loss, in which IGBT loss includes switching loss and conduction loss, which is expressed as follows:

$$\begin{cases} P_{c(T)} = (I_{\text{out}} \cdot (V_{\text{ce0}(25^\circ)} + TC_v \cdot (T_j - 25^\circ))) \\ \qquad + I_{\text{out}}^2 (r_{\text{ce}(25^\text{o})} + TC_r \cdot ((T_j - 25^\circ))) D_{(T)} \\ P_{\text{sw(T)}} = f_s \cdot E_{\text{on+off}} \cdot \left(\frac{I_{\text{out}}}{I_{\text{ref}}}\right)^{Ki} \cdot \left(\frac{V_{\text{in}}}{V_{\text{ref}}}\right)^{Kv} \\ \qquad \cdot (1 + TC_{\text{Esw}} \cdot (T_j - T_{\text{ref}})) \end{cases} \tag{33}$$

where I_{out} is the effective value of load current; $D_{(T)}$ is the duty ratio of IGBT; T_{CV} and T_{Cr} are the temperature factors of the conduction characteristic curve; I_{ref}, V_{ref}, and T_{ref} are the device rated parameters; K_i is the loss factor varying with current; K_v is the loss factor varying with voltage; TC_{Esw} is the loss temperature factor; $E_{\text{on+off}}$ is the sum of the energy losses of the device turn ON and OFF.

TABLE III
PARAMETERS FOR EFFICIENCY ANALYSIS

Item	Value	Item	Value
I_{out}	150A	E_{on}	0.0043J
$D_{(\text{T})}$	0.7	TC_{v}	0.0012
V_{in}	650V	I_{ref}	200A
V_{ce025}	1.38	V_{ref}	450V
$r_{\text{ce}(25^\circ)}$	0.004	TC_{Esw}	0.003
E_{off}	0.0073J	T_{j}	125
TC_{Err}	0.006	T_{ref}	25
K_{iD}	0.6	K_{i}	1.0
K_{vD}	0.6	K_{v}	1.35
TC_{vD}	0.002	E_{rr}	0.0045
I_{refD}	200	V_{refD}	450
P_{rated}	125kW	K_n	4

The body diode loss includes conduction loss and turn OFF loss, which is expressed as

$$\begin{cases} P_{c(D)} = (I_{\text{out}} \cdot (V_{\text{Fe0}(25^\circ)} + TC_v \cdot (T_j - 25^\circ))) \\ \qquad + I_{\text{out}}^2 (r_{F(25^\text{o})} + TC_r \cdot ((T_j - 25^\circ))) D_{(\text{D})} \\ P_{\text{sw}(T)} = f_s \cdot E_{rr} \cdot \left(\frac{I_{\text{out}}}{I_{\text{ref}}}\right)^{Ki} \cdot \left(\frac{V_{\text{in}}}{V_{\text{ref}}}\right)^{Kv} \\ \qquad \cdot (1 + TC_{\text{Err}} \cdot (T_j - T_{\text{ref}})) \end{cases} \tag{34}$$

where $D_{(T)}$ is the duty ratio of body diode; TC_{Err} is the temperature factor of body diode; E_{rr} is the turn OFF energy loss of diode; K_{iD} and K_{vD} are the factors of diode current and voltage varying with temperature, respectively. All the parameters of IGBT and its body diode can be found in the datasheet.

Thus, according to (33) and (34), the efficiency of FCBBC can be expressed as

$$E = 1 - \frac{1}{P_{\text{system}}} \left[(P_{c(T)} + P_{\text{sw}(T)}) \cdot K_n + (P_{c(D)} + P_{\text{sw}(D)}) \cdot K_n \right] \tag{35}$$

where P_{system} is the system rated power, and K_n is the number of switching device in operation.

Taking the Infineon F3L400R10W3S7 IGBT module as the example, the efficiency of the proposed FCBBC are analyzed according to (35), and the detailed parameters are given in Table III.

According to the parameters given in Table III, the efficiency of FCBBC with different conditions is shown in Fig. 18. Fig. 18(a) shows the efficiency of FCBBC when the duty ratio is set to be 0.7 and the switching frequency gradually increases from 10 to 19 kHz. It can be seen that the power loss increases gradually with the increase of switching frequency. The minimum efficiency of the FCBBC is still larger than 98.6%. Fig. 18(b) shows the efficiency curve when the duty ratio gradually increases from 0.1 to 0.9 when the switching frequency is 10kHz. Based on the two efficiency curves shown in Fig. 18, we can see that when FCBBC works with 1300 V/150 A under buck-boost mode, the efficiency is larger than 98.5%.

IV. CONCLUSION

In this article, an FC dc/dc converter with bidirectional four quadrant operation capability is proposed, which can solve the power conversion issue of ESS under the wide dc bus voltage range. The operating principle of the converter is analyzed

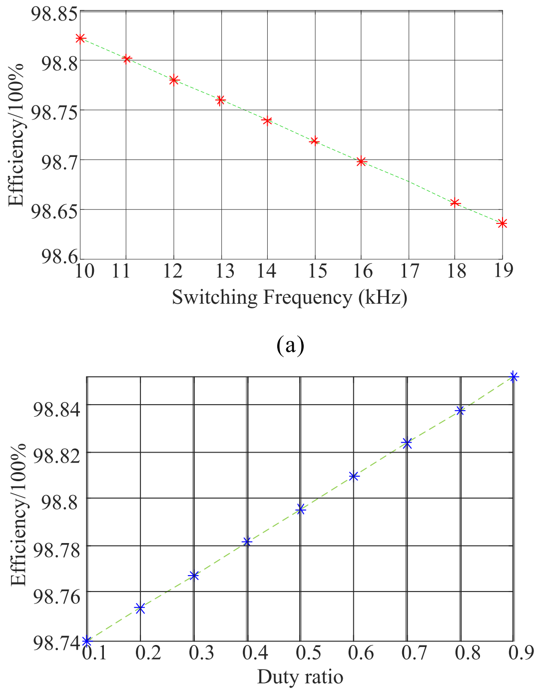

(a)

(b)

Fig. 18. Efficiency of FCBBC. (a) With different switching frequency. (b) With different duty ratios.

in detail, and the mathematical model of FCBBC is studied. According to the ESS operation requirements, a fixed frequency MPC strategy is proposed. The cost function is optimized and the binary search algorithm is adopted to improve the strategy computational efficiency, effectively reduce the computation load, making the proposed MPC strategy more practical. The experimental results show that the ESS based on the proposed converter and MPC strategy can realize bidirectional power conversation with four quadrant, and has favorable control performance. Overall, the proposed FCBBC and MPC strategy have a certain application prospect in the PV station with ESS.

APPENDIX

A. *Voltage Gain of FCBBC*

According to Fig. 3, the converter state equations under Buck mode can be expressed as follows:

$$\text{Fig. 3(a)}\frac{di_L}{dt} = \frac{v1}{L} - \frac{v_{f1}}{L} - \frac{R_L}{L}i_L - \frac{v2}{L} \tag{A1a}$$

$$\text{Fig. 3(b)}\frac{di_L}{dt} = \frac{v1}{L} - \frac{R_L}{L}i_L - \frac{v2}{L} \tag{A1b}$$

$$\text{Fig. 3(c)}\frac{di_L}{dt} = \frac{v_{f1}}{L} - \frac{R_L}{L}i_L - \frac{v2}{L} \tag{A1c}$$

$$\text{Fig. 3(d)}\frac{di_L}{dt} = \frac{R_L}{L}i_L - \frac{v2}{L}. \tag{A1d}$$

TABLE IV
CIRCUIT STATE OPERATION TIME

Mode	Operation time		
	D<0.5	D>0.5	D=0.5
Buck	Fig.3(a):$d_{11}T_s$ Fig.3(c):$d_{11}T_s$, Fig.3(d):(1-2d_{11})T_s	Fig.3(a):(1-d_{11})T_s Fig.3(b):(1-d_{11})T_s Fig.3(c):(2d_{11}-1)T_s	Fig.3(a):$d_{11}T_s$ Fig.3(c):(1-2d_{11})T_s
Boost	Fig.4(a):$d_{24}T_s$ Fig.4(c):$d_{24}T_s$, Fig.4(d):(1-2d_{24})T_s	Fig.4(a):(1-d_{24})T_s Fig.4(b):(1-d_{24})T_s Fig.4(c):(2d_{24}-1)T_s	Fig.4(a):$d_{24}T_s$ Fig.4(c):(1-2d_{24})T_s
Buck-Boost	Fig.5(b):(2d_{11}-1)T_s Fig.5(c):$d_{11}T_s$, Fig.5(d):$d_{11}T_s$	Fig.5(a):(2d_{11}-1)T_s Fig.5(c):(1-d_{11})T_s, Fig.5(d):(1-d_{11})T_s	Fig.5(a):$d_{11}T_s$ Fig.5(c):(1-2d_{11})T_s

According to Fig. 4, we can have the converter state equations under boost mode, which are expressed as

$$\text{Fig. 4(a)}\frac{di_L}{dt} = \frac{v1}{L} + \frac{v_{f2}}{L} - \frac{R_L}{L}i_L - \frac{v2}{L} \tag{A2a}$$

$$\text{Fig. 4(b)}\frac{di_L}{dt} = \frac{v1}{L} - \frac{R_L}{L}i_L \tag{A2b}$$

$$\text{Fig. 4(c)}\frac{di_L}{dt} = \frac{v1}{L} - \frac{R_L}{L}i_L - \frac{v_{f2}}{L} \tag{A2c}$$

$$\text{Fig. 4(d)}\frac{di_L}{dt} = \frac{v1}{L} - \frac{R_L}{L}i_L - \frac{v2}{L}. \tag{A2d}$$

In buck mode, taking the duty ratio less than 0.5 as an example, the converter operating states given in Table I are Fig. 3(a), Fig. 3(c) and (d). According to the switch driving principle, the operation times of the three states are $d_{11}T_s$, $d_{11}T_s$, and (1-2d_{11})T_s, respectively. Thus, multiply the state times with the corresponding (A1a), (A1c), and (A1d), and then add the products to obtain (A3)

$$d_{11}v_1 = v2 - R_L i_L. \tag{A3}$$

Ignoring the equivalent resistance R_L, (A3) is the same as voltage gain of Buck mode shown in (1).

The operation time of each circuit state under different operation modes is given in Table IV. Thus, according to the operation time and the state equation, the same converter voltage gain as (1) can be obtained by using the derivation method of (A3).

B. *Parameters Design*

Because FCBB work with different states under different duty ratio, it is necessary to design the parameters under two conditions, respectively, for comprehendsive selection. Based on the equations shown in (3)–(6) and the working time shown in Table III, we can have the current ripple expression when 0 $< d_{11} <$ 0.5

$$\Delta I_L = \frac{v_1/2 - v_2/2}{L}T_\text{on} = \frac{v_1(1-2d_{11})d_{11}}{2(1-d_{11})Lf_s}. \tag{A4}$$

When 0.5 $< d_{11} <$ 1, the current ripple can be expressed as

$$\Delta I_L = \frac{v_1/2 - v_2/2}{L}T_\text{off} = \frac{v_1(2d_{24}-1)}{2Lf_s}. \tag{A5}$$

It can be known from (A4) and (A5) that when the duty ratio is $1 - 2/\sqrt{2}$ or 1, the current ripple can achieve the maximum value, and the maximum ripple is shown as

$$\Delta I_{L\max} = \frac{v_1}{2Lf_s}. \tag{A6}$$

According to (A6), the minimum inductor value can be obtained, which is the same as that shown in (2).

Similarly, when $0 < d_{11} < 0.5$, the voltage ripple of FC is

$$\Delta v_{\text{fly}} = \frac{i_L}{C_f}T_{\text{on}} = \frac{i_L}{C_f f_s}d_{11}. \tag{A7}$$

When $0.5 < d_{11} < 1$, the voltage ripple of FC is

$$\Delta v_{\text{fly}} = \frac{i_L}{C_f}T_{\text{off}} = \frac{i_L}{C_f f_s}(1 - d_{24}). \tag{A8}$$

According to (A7) and (A8), when the duty ratio approaches 0.5, the voltage ripple of FC reaches the maximum value, and the maximum ripple can be expressed as

$$\Delta v_{\text{flymax}} = \frac{i_L}{2C_f f_s}. \tag{A9}$$

Thus, the minimum value of FC can be obtained form (A9).

REFERENCES

[1] T. Mai *et al.*, "Renewable electricity futures for the United States," *IEEE Trans. Sustain. Energy*, vol. 5, no. 2, pp. 372–378, Apr. 2014.

[2] M. M. Rahman and E. Velayutham, "Renewable and non-renewable energy consumption-economic growth nexus: New evidence from South Asia," *Renewable Energy*, vol. 147, pp. 399–408, Mar. 2020.

[3] K. Sun, L. Zhang, Y. Xing, and J. M. Guerrero, "A distributed control strategy based on DC bus signaling for modular photovoltaic generation systems with battery energy storage," *IEEE Trans. Power Electron.*, vol. 26, no. 10, pp. 3032–3045, Oct. 2011.

[4] X. Li and S. Wang, "A review on energy management operation control and application methods for grid battery energy storage systems," *CSEE J. Power Energy Syst.*, vol. 7, pp. 1026–1040, 2021.

[5] J. Hofer, B. Svetozarevic, and A. Schlueter, "Hybrid AC/DC building microgrid for solar PV and battery storage integration," in *Proc. IEEE 2nd Int. Conf. DC Microgrids*, Jun. 2017, pp. 188–191.

[6] T. S. Babu, K. R. Vasudevan, V. K. Ramachandaramurthy, S. B. Sani, S. Chemud, and R. M. Lajim, "A comprehensive review of hybrid energy storage systems: Converter topologies control strategies and future prospects," *IEEE Access*, vol. 8, pp. 426148702–426148721, 2020.

[7] X. Zhang, B. Wang, U. Manandhar, H. Beng Gooi, and G. Foo, "A model predictive current controlled bidirectional three-level DC/DC converter for hybrid energy storage system in DC microgrids," *IEEE Trans. Power Electron.*, vol. 34, no. 5, pp. 4025–4030, May 2019.

[8] P. J. Grbovic, P. Delarue, P. L. Moigne, and P. Bartholomeus, "A bidirectional three-level DC–DC converter for the ultracapacitor applications," *IEEE Trans. Ind. Electron.*, vol. 57, no. 10, pp. 3415–3430, Oct. 2010.

[9] X. Ruan, B. Li, Q. Chen, S. C. Tan, and C. K. Tse, "Fundamental considerations of three-level dc–dc converters: Topologies analyses and control," *IEEE Trans. Circuits Syst. I, Reg. Papers*, vol. 55, no. 11, pp. 3733–3743, Dec. 2008.

[10] L. Tan, B. Wu, S. Rivera, and V. Yaramasu, "Comprehensive DC power balance management in high-power three-level DC–DC converter for electric vehicle fast charging," *IEEE Trans. Power Electron.*, vol. 31, no. 1, pp. 89–100, Jan. 2016.

[11] H. Chen, C. Lu, W. Lien, and T. Chen, "Active capacitor voltage balancing control for three-level flying capacitor boost converter based on average-behavior circuit model," *IEEE Trans. Ind. Appl.*, vol. 55, no. 2, pp. 1628–1638, Mar./Apr. 2019.

[12] R. Stala, "The switch-mode flying-capacitor DC–DC converters with improved natural balancing," *IEEE Trans. Ind. Electron.*, vol. 57, no. 4, pp. 1369–1382, Apr. 2010.

[13] L. Callegaro, M. Ciobotaru, D. J. Pagano, and J. E. Fletcher, "Control design for photovoltaic power optimizers using bootstrap circuit," *IEEE Trans. Energy Convers.*, vol. 34, no. 1, pp. 232–242, Mar. 2019.

[14] L. Callegaro, M. Ciobotaru, D. J. Pagano, and J. E. Fletcher, "Feedback linearization control in photovoltaic module integrated converters," *IEEE Trans. Power Electron.*, vol. 34, no. 7, pp. 6876–6889, Jul. 2019.

[15] M. Duan, D. Sun, J. Duan, L. Sun, and Y. Liu, "Interleaved modulation scheme with optimized phase shifting for double-switch buck-boost converter," *IEEE Access*, vol. 9, pp. 55422–55435, 2021.

[16] B. P. McGrath and D. G. Holmes, "Analytical modeling of voltage balance dynamics for a flying capacitor multilevel converter," *IEEE Trans. Power Electron.*, vol. 23, no. 2, pp. 543–550, Mar. 2008.

[17] R. Stala *et al.*, "Results of investigation of multicell converters with balancing circuit—Part I," *IEEE Trans. Ind. Electron.*, vol. 56, no. 7, pp. 2610–2619, Jul. 2009.

[18] R. H. Wilkinson, T. A. Meynard, and H. du Toit Mouton, "Natural balance of multicell converters: The two-cell case," *IEEE Trans. Power Electron.*, vol. 21, no. 6, pp. 1649–1657, Nov. 2006.

[19] R. Stala, "The switch-mode flying-capacitor dc-dc converters with improved natural balancing," *IEEE Trans. Ind. Electron.*, vol. 57, no. 4, pp. 1369–1382, Apr. 2010.

[20] A. M. Y. M. Ghias, J. Pou, M. Ciobotaru, and V. G. Agelidis, "Voltage-balancing method using phase-shifted PWM for the flying capacitor multilevel converter," *IEEE Trans. Power Electron.*, vol. 29, no. 9, pp. 4521–4531, Sep. 2014.

[21] A. M. Y. M. Ghias, J. Pou, G. J. Capella, P. Acuna, and V. G. Agelidis, "On improving phase-shifted PWM for flying capacitor multilevel converters," *IEEE Trans. Power Electron.*, vol. 31, no. 8, pp. 5384–5388, Aug. 2016.

[22] G. Farivar, A. M. Y. M. Ghias, J. Pou, and V. G. Agelidis, "Capacitor voltages measurement and balancing in flying capacitor multilevel converters utilizing a single voltage sensor," *IEEE Trans. Power Electron.*, vol. 32, no. 10, pp. 8115–8123, Oct. 2017.

[23] A. Shukla, A. Ghosh, and A. Joshi, "Natural balancing of flying capacitor voltages in multicell inverter under PD carrier-based PWM," *IEEE Trans. Power Electron.*, vol. 26, no. 6, pp. 1682–1693, Jun. 2011.

[24] A. M. Y. M. Ghias, J. Pou, G. J. Capella, V. G. Agelidis, R. P. Aguilera, and T. Meynard, "Single-carrier phase-disposition PWM implementation for multilevel flying capacitor converters," *IEEE Trans. Power Electron.*, vol. 30, no. 10, pp. 5376–5380, Oct. 2015.

[25] Q. Wei, B. Wu, D. Xu, and N. R. Zargari, "Model predictive control of capacitor voltage balancing for cascaded modular DC-DC converters," *IEEE Trans. Power Electron.*, vol. 32, no. 1, pp. 752–761, Jan. 2017.

[26] W. Song, M. Zhong, S. Luo, and S. Yang, "Model predictive power control for bidirectional series resonant isolated DC-DC converters with fast dynamic response in locomotive traction system," *IEEE Trans. Transp. Electrific.*, vol. 6, no. 3, pp. 1326–1337, Sep. 2020.

[27] F. An, W. Song, B. Yu, and K. Yang, "Model predictive control with power self-balancing of the output parallel DAB DC–DC converters in power electronic traction transformer," *IEEE J. Emerg. Sel. Topics Power Electron.*, vol. 6, no. 4, pp. 1806–1818, Dec. 2018.

[28] L. Shi, B. P. Baddipadiga, M. Ferdowsi, and M. L. Crow, "Improving the dynamic response of a flying-capacitor three-level buck converter," *IEEE Trans. Power Electron.*, vol. 32, no. 10, pp. 8115–8123, Oct. 2013.

[29] A. B. Ponniran, K. Orikawa, and J. Itoh, "Minimum flying capacitor for N-level capacitor DC/DC boost converter," *IEEE Trans. Ind. Appl.*, vol. 52, no. 4, pp. 3255–3266, Jul. 2016.

[30] J.-J. E. Slotine *et al.*, *Applied Nonlinear Control*, vol. 199, no. 1, Englewood Cliffs, NJ, USA: Prentice-Hall, 1991.

[31] "Three level bidirectional four quadrant DC/DC converter for 1500VDC energy storage system," 2022. [Online]. Available: https://cn.sungrowpower.com/storagesystem/product/38/59.html

Kaitao Bi received the B.S. degree in electronic information engineering and the M.S. and Ph.D. degrees in electrical engineering from the Harbin University of Science and Technology, Harbin, China, in 2012, 2014, and 2019, respectively.

He was with Jiangnan University, Wuxi, China, as an Associate Professor and a Master Tutor, in 2019. His areas of research interests include multilevel converters, high-power energy storage systems, and control algorithms.

Huayang Lv received the B.S. degree in electrical engineering and automation from the School of Hunan University, Changsha, China, in 2018. He is currently working toward the M.S. degree in electrical engineering with Jiangnan University, Wuxi, China.

His research interests include new energy power conversion system and its control technology.

Liang Chen received the B.Sc. degree from the School of electrical engineering, Anhui Polytechnic University, Wuhu, China, in 2020. He is currently working toward the M. Sc. degree in energy and power engineering with Jiangnan University, Wuxi, China.

His current research interests include renewable energy generation systems and dc–dc conversion.

Jianfei Li received the B.S. and M.S. degrees in electrical engineering from the Huazhong University of Science and Technology, Wuhan, China, in 1996 and 1999, respectively.

He is currently the Vice President of Sineng Electric Company, Ltd., Wuxi, China, and a Master Supervisor with the School of Internet of Things, Jiangnan University, Wuxi, China. His main research interests include photovoltaic generation technologies, energy storage system, and distributed generation systems.

Yixin Zhu (Senior Member, IEEE) received the B.S., M.S., and Ph.D. degrees in electrical engineering from Xi’an Jiaotong University, Xi’an, China, in 2009, 2011, and 2015, respectively.

Since 2016, he has been with Jiangnan University, Wuxi, China, where he is currently with the School of IoT engineering, as an Associate Porfessor. His research interests include the design, control and application of the high-power active power filter, the photovoltaic grid-connected inverter, and also the modeling, analysis and power management of the microgrid.

Wentao Huang received the Ph.D. degree in electrical engineering from Southeast University, Nanjing, China, in 2020.

From January 2018 to January 2019, he was a joint Ph.D. student with the School of Electrical and Data Engineering, University of Technology Sydney, Sydney, NSW, Australia. Since 2020, he has been with Jiangnan University, Wuxi, China, where he is currently a Lecturer with the School of Internet of Things Engineering. His major research interests include permanent magnet machine drives, fault diagnosis, and fault-tolerant control.

Qigao Fan (Member, IEEE) received the Ph.D. degree in mechatronic engineering from the School of Mechatronic Engineering, China University of Mining Technology, Xuzhou, China, in 2013.

Since 2013, he has been with Jiangnan University, Wuxi, China, where he is currently an Associate Professor with the School of Internet of Things Engineering. From September 2018 to September 2019, he was a Visiting Scholar with the Department of Mechanical and Industrial Engineering, University of Toronto. His teaching and research interests include motor control, robotics, intelligent sensors, and IoT technology.